Oxidation mechanism of refractory high entropy alloys Ta-Mo-Cr-Ti-Al with varying Ta content

Authors

S. Schellert [a], B. Gorr [b,*], S. Laube [b], A. Kauffmann [b], M. Heilmaier [b] and H. J. Christ [a]

steven.schellert@uni-siegen.de; bronislava.gorr@kit.edu; stephan.laube@kit.edu; alexander.kauffmann@kit.edu; martin.heilmaier@kit.edu; hans-juergen.christ@uni-siegen.de

Affiliation

[a]Institut für Werkstofftechnik, Universität Siegen, Paul-Bonatz-Str. 9-11, 57068 Siegen, Germany;

[b]Institut for Applied Materials (IAM), Karlsruher Institut für Technologie (KIT), Engelbert-Arnold-Str. 4, 76131 Karlsruhe, Germany

[*] corresponding author
mail: bronislava.gorr@kit.edu B. Gorr

Abstract

The effect of Ta on the oxidation resistance of the alloys Ta_x-$(Mo\text{-}Cr\text{-}Ti\text{-}Al)_{1-x}$ (x = 0; 5; 10; 15; 20 at.%) in air at 1200°C was examined. The oxidation behavior improves continuously with the increasing Ta concentration. Alloys with Ta concentrations Ta $\leq$ 10 at.% exhibit poor oxidation. Severe evaporation of MoO_3 occurred which was quantitatively estimated. The evaporation of MoO_3 is drastically reduced in alloys with the higher Ta concentrations. At 15 and 20 at.% Ta, protective $CrTaO_4$ scales are found. The $CrTaO_4$ scale formed on Ta_{20}-$(Mo\text{-}Cr\text{-}Ti\text{-}Al)_{80}$ grows according to the parabolic rate law as a result of oxygen inward diffusion.

Keywords: refractory high entropy alloy, parabolic rate law, Ta effect, $CrTaO_4$ formation, Mo evaporation

1. Introduction

Refractory high entropy alloys (RHEA) are considered to be promising candidates for high temperature applications beyond the temperature capability of Ni-based superalloys [1]. RHEA which contain elements such as Mo, Ta, W, Nb, Hf and Zr are highlighted because of their high melting points and promising mechanical properties [2–5]. However, the oxidation resistance of many published RHEA is still a major drawback because of the formation of non-protective oxide scales, often present in combination with damaging phenomena such as pesting [6–8] and catastrophic oxidation [9,10]. The classical concept of providing oxidation resistance to high temperature alloys relies on the additions of Cr, Al or Si, which enable the formation of protective Cr_2O_3, Al_2O_3 or SiO_2 layers [11–13]. In our recent studies, an alternative way to protect RHEA has been proposed [14]. This approach is based on the formation of a continuous $CrTaO_4$ layer that protects RHEA from severe corrosion attack. Previously, the oxidation behavior of the equiatomic, $CrTaO_4$-forming Ta-Mo-Cr-Ti-Al was investigated in a temperature range from 500°C to 1500°C [15] and the relevant oxidation mechanism was identified [14]. High oxidation resistance of this alloy was observed at least up to 300h at 1000°C. A mass change of just 3.4 mg/cm² was measured under these oxidation conditions [14].
Similarly, Lo et al. [16] reported on the formation of a continuous $CrTaO_4$ layer on the alloy 25.2Cr-17.6Al-20.3Mo-15.2Nb-2.9Si-13.4Ta-5.4Ti (at. %) during long-term exposure up to 200h at 1100°C. Moreover, these $CrTaO_4$ scales were observed on alloys derived from the Ta-Mo-Cr-Ti-Al system. Li-Chao et al. [17] reported the formation of a protective layer after oxidation on the Ta-Mo-Cr-Ti for 10h at 1000°C. It has been proved by Mueller et al. [14] that the formation and stability of $CrTaO_4$ layers strongly depend on the chemical composition of the alloy. The removal of Ti, for example, led to a dramatic decreasing of the oxidation resistance as a $CrTaO_4$ layer, which initially formed on the alloy Ta-Mo-Cr-Al, fails after approximately 40h oxidation at 1000°C [14].

Obviously, Cr and Ta are the key elements to form the protective $CrTaO_4$. It is, therefore, of particular interest to determine the critical concentrations of Ta and Cr required for the formation of a continuous $CrTaO_4$ scale in alloys within the system Ta_x-$(Mo$-Cr-Ti-$Al)_{1-x}$. Apart from the chemical effect of these two elements on the oxidation products, Cr and Ta promote the formation of undesired Laves phase (Cr_2Ta) in RHEA [18–20], which are usually known to be brittle, thus deteriorating room temperature mechanical properties. Therefore, knowledge about the minimum concentrations of Ta and Cr allowing the formation of a $CrTaO_4$ layer is indispensable to achieve a reasonable balance between mechanical properties and oxidation resistance.

In this paper, the effect varying Ta concentrations on the oxidation behavior of Ta_x-$(Mo$-Cr-Ti-$Al)_{1-x}$ (x = 0; 5; 10; 15; 20 at.%) alloys is studied. The Ta content is gradually reduced from the equiatomic Ta-Mo-Cr-Ti-Al alloy to the equiatomic Ta-free alloy Mo-Cr-Ti-Al. Any potential Mo loss as a result of the formation of volatile MoO_3 is quantitatively estimated for all alloys, which allows the correct evaluation of thermogravimetric data. Using results of oxidation kinetics as well as microstructural investigations, the oxidation mechanisms are identified. Finally, the minimum Ta concentration enabling the formation of a continuous $CrTaO_4$ layer is determined.

2. Experimental Procedures

The alloys for the oxidation experiments were produced using an AM/0.5 arc melting furnace by the company Edmund Bühler GmbH. The pure elements Ta, Mo, Cr, Ti, Al with purities of 99.9, 99.95, 99.99, 99.8, and 99.99%, respectively, were weighed according to the alloy composition, mixed and then melted under an Ar atmosphere. The buttons were turned at least five times in the water-cooled Cu mold and melted again to achieve sufficient homogenization. They were finally drop cast into a rod-shaped Cu mold. To dissolve the dendritic microstructure, the buttons were homogenized at 1500°C for 20h (except Mo-Cr-Ti-Al, which was homogenized at 1200°C for 20h) in Ar atmosphere and slowly cooled inside the furnace. The heating and cooling rate of the furnace was 250 K/h. Samples were taken by electrical discharge machining (EDM). The chemical composition of the investigated alloys is presented in Table 1. The compositions of equiatomic Mo-Cr-Ti-Al and Ta-Mo-Cr-Ti-Al were determined by inductively coupled plasma optical emission spectrometry (ICP-OES) whereas the composition of Ta_x-$(Mo$-Cr-Ti-$Al)_{1-x}$ (x = 5, 10, 15 at.%) were analyzed by standard-related EDX which coincides well with the ICP-OES technique. Note, the maximum deviation for individual elements from the nominal composition is 0.5 at.%. The samples for the oxidation experiments were ground and polished to P4000. The parallelism of the samples, which was required to determine the Mo mass loss during oxidation, was checked with an optical microscope. Before the oxidation tests, the samples were ultrasonically cleaned in ethanol. The high temperature oxidation tests were carried out in a Rubotherm thermogravimetric system (TGA) for 24h at 1200°C in laboratory air. Additionally, selected samples were statically exposed in the furnace for 30 min at the same temperature in order to investigate the oxidation behavior in the initial stage. Various methods were performed to characterize the oxide layers. X-Ray diffraction (XRD) utilizing an X'Pert Pro MPD diffraction device with Cu-Kα radiation was applied to determine the crystal structure of the oxidation products and the lattice parameter. The lattice parameter was calculated by extrapolating using the weighting function $0.5(cos^2\Theta + cot\Theta \cdot cos\Theta)$ adopted from Nelson-Riley [21]. Calibrated TEM-SAD (transmission electron microscopy - selected area diffraction) images of the alloys were taken to verify the calculated lattice parameters a. By measuring the distances d_{hkl} between two adjacent diffraction spots, using the relation $d_{hkl} = \frac{a}{\sqrt{h^2+k^2+l^2}}$, the lattice parameter for the bcc crystal is calculated. For TEM-SAD studies, circular discs with a diameter of 3 mm were ground to a thickness of 100 µm. Finally, the specimens were jet-polished with TenuPol-5 by Struers GmbH at room temperature. Thinning was performed at a voltage of 12 V using an electrolyte consisting of H_2SO_4 and methanol in a ratio of 1 : 4. The following TEM investigations were performed with FEI Talos F200X with 200 kV acceleration voltage. A Focused Ion Beam - Scanning Electron Microscope (FIB-SEM) DualBeam system of type FEI Helios Nanolab 600 equipped with techniques such as backscatter electron (BSE) imaging, energy-dispersive X-ray spectroscopy (EDX) was used to characterize the oxide morphology. The oxide layer thickness and the areal fraction of phases were determined using the BSE images. Assuming isotropy and isometry, the areal fractions after binarization can directly be converted into volume fractions. Approximately 20 thickness measurements were performed for each image using the software ImageJ. To identify the oxidation mechanism and in particular to determine the direction of layer growth, two markers were placed on selected samples by FIB. The FIB marker method is described in detail in Material S2.

3. Results

3.1 Microstructure

Results of experimental studies on the microstructure of the equiatomic alloys Mo-Cr-Ti-Al and Ta-Mo-Cr-Ti-Al were already published and can be found in Refs. [14,18–20,22]. Therefore, the microstructure of the alloys relevant for this study in the homogenized condition is only briefly discussed here. Results of the XRD analyses (Fig. S. 1) reveal that the matrix of all alloys consists of an ordered B2 crystal structure. This finding is confirmed by TEM investigations carried out on the equiatomic Mo-Cr-Ti-Al and Ta-Mo-Cr-Ti-Al alloy [20].

BSE images illustrated in Fig. 1 reveal the Cr_2Ta Laves phase C14 (bright contrast) at the grain boundaries of Ta_{10}-(Mo-Cr-Ti-Al)$_{90}$, Ta_{15}-(Mo-Cr-Ti-Al)$_{85}$ and equiatomic Ta-Mo-Cr-Ti-Al [18,20]. In Fig. 1 (f.), the volume fraction of the Laves phase for the same homogenization and cooling conditions is plotted versus the Ta concentration. It highlights that at 5 at.% Ta and below, the investigated alloys are free of the (secondary) Laves phase, hence a single phase microstructure is assumed. Above this threshold concentration the volume fraction of the Laves phase increases slightly and is still approximately 0.4 vol.% for the equiatomic Ta-Mo-Cr-Ti-Al. It should be mentioned, however, that the alloys are not in thermodynamic equilibrium, even after heat treatment.

3.2 Oxidation kinetics

Figure 2 (a.) depicts the specific mass change curves of all investigated alloys during isothermal exposure to laboratory air at 1200°C for 24h. The oxidation curves are obviously strongly dependent on the Ta content. The Mo-Cr-Ti-Al alloy exhibits complex oxidation kinetics with alternating intervals of mass gains and mass losses. After 24 hours of exposure, this alloy yields a negative mass change in total. The mass change of the alloy with 5 at. % Ta shows a first mass gain up to about 7h, afterwards however, continuous mass loss was recorded. Alloys with Ta concentrations higher than 5 at.% exhibit continuous mass gains during the entire exposure time. Surprisingly, the Ta_{15}-(Mo-Cr-Ti-Al)$_{85}$ alloy yields the lowest mass gain, while the highest was detected for the alloy with 10 at.% Ta. In order to prove reproducibility, the experiments of the Ta-containing alloys Ta_x-(Mo-Cr-Ti-Al)$_{1-x}$ (x = 5; 10; 15; 20 at.%) at 1200°C were repeated and the results can be found in Fig. S. 2. All thermogravimetric curves are reproducible and reveal the same trends.

3.3 Oxide scales

In order to identify the crystal structure of corrosion products formed on alloys during oxidation at 1200°C for 24h, XRD analyses were carried out. Figure 3 (a.) exemplifies the corresponding XRD patterns for all investigated alloys. The results indicate that TiO_2, Al_2O_3 and Cr_2O_3 form on all alloys. $CrTaO_4$ was additionally detected on 15Ta-Mo-Cr-Ti-Al and equiatomic Ta-Mo-Cr-Ti-Al. The $CrTaO_4$ oxide on the equiatomic Ta-Mo-Cr-Ti-Al reveals lattice constants of a = 4.635 Å and c = 3.011 Å. Compared to those of pure $CrTaO_4$ (a = 4.642 Å, c = 3.020 Å, PDF No. 39-1428 [23]), the a and c axis are upset by 0.15 % and 0.30 %.

Further, a yellow substance was detected on the platinum wire of the cool zone of the thermogravimetric system after oxidation in all cases. The amount of this substance increases with decreasing Ta content in the respective alloys. In order to identify the nature of the substance, it was removed after oxidation of the alloy Ta_{15}-(Mo-Cr-Ti-Al)$_{85}$. The XRD analysis (see Fig. 3 b.) reveals the sole presence of MoO_3. Apparently, vaporization of Mo oxide(s) takes place during oxidation.

Cross-section micrographs of all alloys after 24h oxidation in air at 1200°C are presented in Fig. 4. All oxide scales generally exhibit a multi-layer structure. The outermost oxide scale formed on all alloys consists of Al_2O_3 and TiO_2, whereby the Al_2O_3 fraction seems to increase with increasing Ta concentration. Underneath, TiO_2 scale with embedded Cr_2O_3 particles was identified in all cases. Locally, Cr_2O_3 forms a semi-continuous net which becomes more pronounced with increasing Ta content.

Below these layers, the oxide scales can be classified in two groups depending on the Ta content. Mo-Cr-Ti-Al, Ta_5-(Mo-Cr-Ti-Al)$_{95}$, Ta_{10}-(Mo-Cr-Ti-Al)$_{90}$ form thick and porous scales that represent a mixture of Ti-, Al-, Cr-oxides (Fig. 4 a.-c.). Underneath the thick oxide layers, a relatively thin zone of internal corrosion with spherical Al_2O_3 and needle-shaped TiN particles was observed. In contrast, Ta_{15}-(Mo-Cr-Ti-Al)$_{85}$ and equiatomic Ta-Mo-Cr-Ti-Al exhibit a rather thin rutile type $CrTaO_4$ layer (Fig. 4 d.-e.). Beneath the $CrTaO_4$ layer, a thick zone of internal corrosion with Al_2O_3 and TiN particles was identified in alloys with 15 and 20 at.% Ta.

The equiatomic Ta-Mo-Cr-Ti-Al reveals the thinnest $CrTaO_4$ layer. To obtain further information about the chemical composition of the $CrTaO_4$ layer, a TEM lamella was extracted from the substrate/oxide interface on equiatomic Ta-Mo-Cr-Ti-Al using FIB lift out. In Fig. 5, a continuous $CrTaO_4$ layer is highlighted by a blue frame. The corresponding EDX mapping (Fig. 5 b.) reveals that the $CrTaO_4$ layer containing considerable amounts of Ti (approx. 12 at.%).

In order to assess the protectiveness of oxide layers formed on the alloys studied, the thicknesses of the oxide scales as well as those of the internal corrosion zones are summarized in Fig. 6. Apparently, the oxide scales become progressively thicker with decreasing Ta content. Whereas this progress is more pronounced for the alloys with Ta concentrations between 0 and 10 at.%, the thickness difference between alloys with 15 and 20 at.% is only marginal. It could, therefore, be assumed that the protective effect of the oxide scale is significantly improved if the Ta concentration in the alloy exceeds 10 at.%.

In general, Ta seems to play the dominant role in the oxidation resistance of Ta_x-(Mo-Cr-Ti-Al)$_{1-x}$ as the oxide scale formed on the Ta-free alloy after 24h of oxidation at 1200°C is about one order of magnitude thicker compared to that formed on the equiatomic Ta-Mo-Cr-Ti-Al. The thickness of the internal corrosion zone increases with the increasing Ta content up to 10 at.%. In alloys with a higher Ta concentration, i.e. 15 and 20 at.%, the thickness of the zone of internal corrosion, on the contrary, slightly decreases with increasing Ta content. The smallest depth of internal corrosion is observed for the Ta-free alloy, while the most pronounced internal corrosion is found in Ta_{10}-(Mo-Cr-Ti-Al)$_{90}$.

In order to shed light on the oxidation mechanisms, information about growth direction with respect to the initial sample surface is required. The determination of the original sample surface was performed for two alloys, i.e. Ta_5-(Mo-Cr-Ti-Al)$_{95}$ and Ta_{20}-(Mo-Cr-Ti-Al)$_{80}$, as these alloys exhibited different structures of the oxide layers, which are typical of the alloys under investigation. The alloys Mo-Cr-Ti-Al and Ta_{10}-(Mo-Cr-Ti-Al)$_{90}$ oxidize similar to the former (see Fig. 4 a.-c.), while the oxide scale formed on Ta_{15}-(Mo-Cr-Ti-Al) resembles that of the latter alloy (see Fig. 4 e.-f.).

Two circular FIB markers were placed 50 µm and 100 µm away from the surface on the alloy Ta_5-(Mo-Cr-Ti-Al)$_{95}$ and equiatomic Ta-Mo-Cr-Ti-Al, respectively (see Fig. 7). The markers were located parallel to the sample surface. The distances between the markers and the sample surfaces were chosen in consideration of the expected thickness after corrosion attack. The corresponding markers and, therefore, the original sample surfaces were then easily identified in the alloys Ta_5-(Mo-Cr-Ti-Al)$_{95}$ and equiatomic Ta-Mo-Cr-Ti-Al which were oxidized at 1200°C for 30 min and 24h, respectively.

In case of Ta_5-(Mo-Cr-Ti-Al)$_{95}$, top Al_2O_3, Cr_2O_3 and TiO_2 grow as a result of cation outward diffusion, while the inner scale consisting of a mixture of Al-, Cr- and Ti- oxides (compare with Fig. 4) grows due to the inward oxygen diffusion. Similarly, the outer layer including Cr_2O_3, Al_2O_3 and TiO_2 grows outward on equiatomic Ta-Mo-Cr-Ti-Al. The $CrTaO_4$ layer grows at the interface oxide/substrate as a result of oxygen inward transport. Using this method, it is, however, difficult to state whether the semi-continuous Cr_2O_3, which is located adjacent above the $CrTaO_4$ layer, grows due to cation or anion diffusion as this scale is very thin.

To investigate the growth kinetics of oxides formed on equiatomic Ta-Mo-Cr-Ti-Al in more detail, the thicknesses of the outer scale consisting of TiO_2, Al_2O_3 and Cr_2O_3 layers, the $CrTaO_4$ layer as well as the zone of internal corrosion after exposure for 8h, 12h and 24h were measured and displayed in Fig. 8. Apparently, the thickness of the outer layer remains almost constant. This observation confirms our earlier investigations that the outer scale consisting of TiO_2, Al_2O_3 and Cr_2O_3 forms during transient oxidation and does not significantly change during the steady-state oxidation [14,24]. It should be noted here that the rather large scatter of the outer oxide layer thickness is attributed to a non-uniform whisker-like formation of TiO_2 (see Fig. 4 e.). As clearly depicted in Fig. 8, the thickness of the zone of internal corrosion of the equiatomic Ta-Mo-Cr-Ti-Al increases significantly during oxidation. TiN and Al_2O_3 were identified as corrosion products that indicate that both, oxygen and nitrogen can easily diffuse through the $CrTaO_4$ scale. It should be mentioned that, like in the case of the outer oxide layer, the rather large scatter resume due to the need-like shape TiN.

4. Discussion

Our previous investigations showed that the equiatomic alloy Ta-Mo-Cr-Ti-Al exhibits high oxidation resistance in a wide temperature range from 500 to 1500°C as low mass changes and thin oxide scales were observed [15]. Müller et al. identified the oxidation mechanism of this alloy and proved that the slow oxygen diffusion through continuous $CrTaO_4$ layer is responsible for the superior oxidation resistance [14]. Based on our previous results, it can, therefore, be assumed that the oxidation behavior of $(Ta)_x$-$(Mo\text{-}Cr\text{-}Ti\text{-}Al)_{1-x}$ (x = 0; 5; 10; 15; 20) is strongly influenced by the formation of the $CrTaO_4$ layer.

The experimental results from the present study reveal that the oxidation behavior changes in $(Ta)_x$-$(Mo\text{-}Cr\text{-}Ti\text{-}Al)_{1-x}$ alloys with increasing Ta content. Alloys with 15 and 20 at.% Ta form relatively protective $CrTaO_4$ layers at the interface oxide/metal. In contrast, a content below 15 at.% Ta is not sufficient to form $CrTaO_4$ oxide. Despite the high Cr and Al concentrations, i.e. 25 at.% each element, neither protective continuous Cr_2O_3 [25] nor Al_2O_3 [26] scales were found on Mo-Cr-Ti-Al. This underpins the key role of the element Ta on the protective $CrTaO_4$.

The formation of rutile-type $CrTaO_4$ as a product of the reaction between Ta_2O_5 and Cr_2O_3 was reported in limited amount of studies [14,24,27,28]. For example, Brady et al. [29] reported on the formation of an approximately 20 µm thick $CrTaO_4$ scale on the model alloy Cr_{80}-Ta_{20} (at.%) after 24h of oxidation at 1100°C. A beneficial effect of $CrTaO_4$ was also identified in Ni-based superalloys [24,30,31]. In this multicomponent alloy system, only 5 wt.% (1.7 at.%) Ta and 8 wt.% (9.1 at.%) Cr are sufficient for the formation of a $CrTaO_4$ layer [30]. By increasing the Ta content up to 1.9 at.%, an even lower mass gain was observed [30]. Furthermore, it should be mentioned that the Ti concentration in this alloy is 2 wt.% (2.5 at.%). Jalowicka et al. report that the nickel-base superalloy PWA 1483 with a Ta concentration of 5 wt.% (1.7 at.%), Cr content of 12 wt.% (13.5 at.%) and higher Ti content 5 wt.% (5.1 at.%) forms a rutile-type $TaTiO_4$ oxide after 20h oxidation in synthetic air at 1050°C [32].

Obviously, these low Ta concentrations leading to the formation of a continuous $CrTaO_4$ layer in Ni-based superalloys are too low in case of the RHEA investigated here. Thus far, only few publications were counted in literature that identified $CrTaO_4$ in RHEA [16,33]. Recently, Lo et al. [16] found that the RHEA 25.2Cr-17.6Al-20.3Mo-15.2Nb-2.9Si-13.4Ta-5.4Ti (at.%) in the as-cast condition forms a $CrTaO_4$-based oxide which protects the alloy from catastrophic oxidation during 200h exposure at 1100°C.

Moreover, Lo et al. [16] determined the lattice parameters (a = 4.63 Å, c = 2.997 Å) of the rutile-type $CrTaO_4$-based oxide and found that the lattice parameters differ from those of pure $CrTaO_4$ presumably due to the dissolution of other elements (7 at.% Al, 0.2 at.% Si, 3.9 at.% Ti, 6.3 at.% Nb, and 2.8 at.% Mo) in $CrTaO_4$ [16]. It is well-known that Al, Cr, Ti in combination with Ta can form various rutile-type oxides such as $AlTaO_4$ [34], $CrTaO_4$ [24] as well as $TiTaO_4$ [35]. Further, the successful synthesis of rutile-type $AlTaTiO_6$ and $CrTaTiO_6$ was reported in Ref. [36]. It should be stressed that the reported lattice parameters of $CrTaTiO_6$ (lattice parameter a = 4.633 Å, c = 3.003 Å, [36]) and those of $CrTaO_4$ (a = 4.642 Å, c = 3.020, PDF No. 39-1428 [23]) are very similar.

Apparently, the lattice parameters of $CrTaO_4$ (a = 4.635 Å and c = 3.011 Å) grown on the equiatomic Ta-Mo-Cr-Ti-Al investigated in this study are between those of pure $CrTaO_4$ and those of $CrTaTiO_6$. It can be assumed that the shift in the lattice parameters from pure $CrTaO_4$ towards $CrTaTiO_6$ can be attributed to the high Ti content detected in the Cr-Ta-based oxide grown on the present equiatomic RHEA (see STEM-EDX mapping Fig. 5). It could further be speculated that $CrTaTiO_6$ can form on RHEA within the Ta-Mo-Cr-Ti-Al system with a higher Ti concentrations instead of $CrTaO_4$. Further in-depth studies are necessary to shed light on the protective properties of rutile-type Cr-Ta-(Ti) oxides such as $CrTaTiO_6$ and $CrTaO_4$.

In order to quantify the growth kinetics of $CrTaO_4$, the thickness of the $CrTaO_4$ layer formed on the equimolar Ta-Mo-Cr-Ti-Al alloy was measured after 8, 12 and 24h of oxidation at 1200°C. The results are plotted versus time in double logarithmic form in Fig. 9. In addition, the mass change recorded during oxidation of this alloy is also depicted in Fig. 9. The $CrTaO_4$ layer obviously grows according to a parabolic rate law as the slope of ½ of the straight line confirms. In combination with the results of the marker experiment (see Fig. 7), it can be concluded that $CrTaO_4$ grows parabolically at the metal-oxide interface as a consequence of the inward oxygen diffusion.

Further, it is of a particular interest to investigate whether dense $CrTaO_4$ layers can prevent severe evaporation of refractory metal oxides. As shown above, the TGA curves, the XRD results and the EDX mappings (see also Supplementary Material S1 Fig. S. 3 and Fig. S. 4) reveal that evaporation of MoO_3 takes place in all alloys under investigation. It is well-known that Mo forms volatile MoO_3 above 800°C [9,37,38] strongly influencing the recorded mass change in the TGA. Consequently, the Mo loss as a result of the MoO_3 (g) formation was calculated for each alloy oxidized for 24h at 1200°C. In this calculation it was assumed that Mo entirely evaporates in the zone between the substrate/oxide interface and the original sample surface, which was determined using the FIB markers in Fig. 7. The method applied to determine the Mo mass loss is described in detail in Supplementary Material S2.

As a result Fig. 10 (a.) clearly shows that the calculated mass loss by evaporation decreases strongly with the increasing Ta content. The equiatomic Ta-Mo-Cr-Ti-Al alloy yields the lowest value of only approximately 0.4 mg/cm² after 24h of oxidation at 1200°C. The calculated mass loss (Fig. 10 (a.)) was then subtracted from the recorded overall mass change (Fig. 2) to reveal the actual oxidation kinetics in terms of the oxygen uptake and formation of solid oxides on the sample surface. Fig. 10 (b.) compares the recorded mass change with the calculated mass gain taking into account the determined values of the Mo loss.

The importance of the consideration of the Mo mass loss for interpreting the thermogravimetric data becomes particularly evident in case of the equiatomic Mo-Cr-Ti-Al alloy. This alloy revealed a marginally negative mass change of about 2 mg/cm^2, while the oxygen uptake by solid oxides yields 73 mg/cm^2 after 24h exposure to air at 1200°C. This finding is in accordance with the microstructural observations, as this alloy exhibits the thickest oxide scales (see Fig. 4). The alloy with 15 at.% Ta showed the lowest recorded positive mass change (see Fig. 2). However, the lowest mass gain by scale formation is found for the equiatomic Ta-Mo-Cr-Ti-Al alloy. Again, the oxygen uptake is in agreement with the microstructural observations of the oxide scales illustrated in Fig. 4.

Generally, it can be stated that the difference between the measured and calculated mass change continuously decreases with increasing Ta content and almost vanishes for the equiatomic, Ta-containing alloy. This trend can be clearly attributed to the dependence of the Mo loss on the Ta content in the alloys (see Fig. 10 (a.)). It can further be concluded that the protectiveness of the oxide layers formed on alloys studied is improved with increasing Ta concentration.

Both, the results and discussion presented above allow the conclusion that a protective $CrTaO_4$ layer forms and protects the substrate from catastrophic oxidation if the Ta concentration exceeds 10 at.%. Ta_{15}-(Mo-Cr-Ti-Al)$_{85}$ and equiatomic Ta-Mo-Cr-Ti-Al form distinctively multi-layer scales consisting of an outer scale, which includes TiO_2, Al_2O_3 and Cr_2O_3, and a $CrTaO_4$ scale at the interface oxide/substrate. Both alloys are protected by the slowly growing $CrTaO_4$ layers, which grow inward as a result of the oxygen diffusion. The thickness of the outer scale does not change during steady-state oxidation indicate of a formation within the initial stage of oxidation (see Fig. 6).

If comparing the two alloys, equiatomic Ta-Mo-Cr-Ti-Al forms a more protective $CrTaO_4$ layer, because: (i) the thinner oxide scale (see Fig. 4), (ii) the lower mass loss by evaporation (see Fig. 10) and (iii) a less pronounced zone of internal corrosion (see Fig. 6) were identified in this alloy.

If the Ta concentration is below 15 at.%, the alloy is not able to form a protective $CrTaO_4$ film. The relatively thin outer layer consisting of TiO_2, Al_2O_3 and Cr_2O_3 is similar to that formed on the alloys with the higher Ta concentrations. The heterogeneous mixture of oxides grows quickly at the interface oxide/metal. The MoO_3 evaporation additionally creates new paths for the ingress of oxygen that accelerates the oxidation of the metal substrate even further. The growth of the oxide scale proceeds faster than that of the zone of internal corrosion because no protective oxide layer can be formed, which prevents the inward diffusion. As a result, the zone of internal corrosion becomes less prominent. Oxide scale growth dominates and comes to the fore.

Fig. 11 schematically summarizes the oxidation mechanism of (a.) $Ta_{0\text{-}10}$-(Mo-Cr-Ti-Al)$_{100\text{-}90}$ (in at.%) and (b.) $Ta_{15\text{-}20}$-(Mo-Cr-Ti-Al)$_{85\text{-}80}$ (in at.%) during exposure at 1200°C. The left image displays the schematic microstructure after 30min and the right after 24h of exposure to air. The different oxides and their respective positions are displayed by schematic geometric symbols of various grayscales and hatchings. The evaporation of MoO_3 (g) is displayed by arrows.

5. Conclusions

In this work, the effect of Ta on the high temperature oxidation behavior of refractory high entropy alloys Ta_x-(Mo-Cr-Ti-Al)$_{1-x}$ (x = 0; 5; 10; 15; 20 at.%) was investigated. The main findings can be summarized as follows:

(i) The oxidation resistance of alloys studied substantially improves with increasing Ta concentration from 0 to 20 at.% during oxidation in air at 1200°C. In particular, the thickness of the oxides scales formed on the alloys and the Mo loss due to the MoO_3 evaporation continuously reduce with the increasing Ta content in the alloys. In particular, the oxidation mechanism changes if the Ta concentration exceeds 10 at.%.

(ii) Alloys with 15 and 20 at.% Ta yield very moderate values of the mass gain, i.e. 3.5 and 4.5 mg/cm^2, respectively, after 24h exposure to air at 1200°C. Both alloys form protective $CrTaO_4$ layers at the interface oxide/metal in addition to the outer scale consisting of discontinuous TiO_2, Al_2O_3 and Cr_2O_3. The dense $CrTaO_4$ layer grows according to a parabolic rate law as a result of the oxygen inward diffusion. The outward diffusion of metal cations is prohibited to a large extent. However, a distinct zone of internal oxidation of Al_2O_3 and TiN is detected in both alloys. The equiatomic Ta-Mo-Cr-Ti-Al possesses superior oxidation resistance as it forms the thinnest oxide scales and the evaporation of MoO_3 is negligible.

(iii) While oxidation kinetics with an overall weight gain was detected for the alloy Ta_{10}-(Mo-Cr-Ti-Al)$_{90}$ during the whole oxidation time, alloys with 5 and 0 at.% Ta reveal intervals with positive and negative mass changes. The negative oxidation kinetics with weight losses is attributed to the evaporation of MoO_3 which was found being the highest for the Ta-free alloy.

(iv) Based on the experimental findings demonstrated in this work, it can be concluded that about 15 at.% Ta is required to ensure an adequate level of the oxidation resistance in the alloy system Ta-Mo-Cr-Ti-Al.

In our further investigations, the effects of Ti and Cr on the high temperature corrosion resistance will be studied. In-depth TEM-EELS (transmission electron microscopy – electron energy loss spectroscopy) in combination with XPS (X-ray photoelectron spectroscopy) studies are planned to elucidate the nature of $CrTaO_4$ based oxide and its properties.

Acknowledgment

The financial support by Deutsche Forschungsgemeinschaft (DFG), grant no. GO 2283/4-2 and HE 1872/34-2 is gratefully acknowledged. Part of this work was performed at the Micro- and Nanoanalytics Facility (MnaF) of the University of Siegen.

Author contributions

Steven Schellert: Writing - Original Draft, Validation, Formal analysis, Investigation, Visualization
Bronislava Gorr: Conceptualization, Visualization, Supervision, Project administration, Funding acquisition, Writing – Review & Editing
Stephan Laube: Validation, Formal analysis
Alexander Kauffmann: Formal analysis, Resources, Visualization, Writing – Review & Editing
Martin Heilmaier: Conceptualization, Resources, Funding acquisition, Writing – Review & Editing
Hans-Jürgen Christ: Conceptualization, Resources, Writing – Review & Editing

Data availability

The data that support the finding of this study are available as supplementary materials or from the corresponding author upon reasonable request.

References

[1] O.N. Senkov, G.B. Wilks, D.B. Miracle, C.P. Chuang, P.K. Liaw, Refractory high-entropy alloys, Intermetallics 18 (2010) 1758–1765. https://doi.org/10.1016/j.intermet.2010.05.014.
[2] O.N. Senkov, J.M. Scott, S.V. Senkova, D.B. Miracle, C.F. Woodward, Microstructure and room temperature properties of a high-entropy TaNbHfZrTi alloy, Journal of Alloys and Compounds 509 (2011) 6043–6048. https://doi.org/10.1016/j.jallcom.2011.02.171.

[3] O.N. Senkov, G.B. Wilks, J.M. Scott, D.B. Miracle, Mechanical properties of Nb25Mo25Ta25W25 and V20Nb20Mo20Ta20W20 refractory high entropy alloys, Intermetallics 19 (2011) 698–706. https://doi.org/10.1016/j.intermet.2011.01.004.

[4] O.N. Senkov, S.V. Senkova, C. Woodward, Effect of aluminum on the microstructure and properties of two refractory high-entropy alloys, Acta Materialia 68 (2014) 214–228. https://doi.org/10.1016/j.actamat.2014.01.029.

[5] D.B. Miracle, O.N. Senkov, A critical review of high entropy alloys and related concepts, Acta Materialia 122 (2017) 448–511. https://doi.org/10.1016/j.actamat.2016.08.081.

[6] M. Azim, S. Burk, B. Gorr, H.-J. Christ, D. Schliephake, M. Heilmaier, R. Bornemann, P.H. Bolívar, Effect of Ti (Macro-) alloying on the high-temperature oxidation behavior of ternary Mo–Si–B alloys at 820–1.300 °C, Oxidation of Metals 80 (2013) 231–242. https://doi.org/10.1007/s11085-013-9375-1.

[7] D. Schliephake, A. Kauffmann, X. Cong, C. Gombola, M. Azim, B. Gorr, H.-J. Christ, M. Heilmaier, Constitution, Oxidation and creep of eutectic and eutectoid Mo-Si-Ti alloys, Intermetallics 104 (2019) 133–142. https://doi.org/10.1016/j.intermet.2018.10.028.

[8] D. Schliephake, M. Azim, K. von Klinski-Wetzel, B. Gorr, H.-J. Christ, H. Bei, E.P. George, M. Heilmaier, High-temperature creep and oxidation behavior of Mo-Si-B alloys with high Ti contents, Metallugical and Materials Transactions A 45 (2014) 1102–1111. https://doi.org/10.1007/s11661-013-1944-z.

[9] E. A. Gulbransen, K. F. Andrew and F. A. Brassart, Oxidation of molybdenum 550° to 1700°C, Journal of The Electrochemical Society 9 (1963) 952-959.

[10] J. Spyridelis, P. Delavignette, S. Amelinckx, On the superstructures of Ta_2O_5 and Nb_2O_5, physica status solidi b 19 (1967) 683–704. https://doi.org/10.1002/pssb.19670190220.

[11] X.H. Wang, Y.C. Zhou, High-temperature oxidation behavior of Ti2AlC in air, Oxidation of Metals 59 (2003) 303-320. https://doi.org/10.1023/A:1023092027697.

[12] Y. Hua, Z. Rong, Y. Ye, K. Chen, R. Chen, Q. Xue, H. Liu, Laser shock processing effects on isothermal oxidation resistance of GH586 superalloy, Applied Surface Science 330 (2015) 439–444. https://doi.org/10.1007/s11837-015-1560-z.

[13] M. Azim, D. Schliephake, C. Hochmuth, B. Gorr, H.-J. Christ, U. Glatzel, M. Heilmaier, Creep resistance and oxidation behavior of novel Mo-Si-B-Ti alloys, JOM 67 (2015) 2621–2628. https://doi.org/10.1007/s11837-015-1560-z.

[14] F. Müller, B. Gorr, H.-J. Christ, J. Müller, B. Butz, H. Chen, A. Kauffmann, M. Heilmaier, On the oxidation mechanism of refractory high entropy alloys, Corrosion Science 159 (2019) 108161. https://doi.org/10.1016/j.corsci.2019.108161.

[15] B. Gorr, F. Müller, S. Schellert, H.-J. Christ, H. Chen, A. Kauffmann, M. Heilmaier, A new strategy to intrinsically protect refractory metal based alloys at ultra high temperatures, Corrosion Science 166 (2020) 108475. https://doi.org/10.1016/j.corsci.2020.108475.

[16] K.-C. Lo, Y.-J. Chang, H. Murakami, J.-W. Yeh, A.-C. Yeh, An oxidation resistant refractory high entropy alloy protected by $CrTaO_4$-based oxide, Scientific reports 9 (2019) 7266. https://doi.org/10.1038/s41598-019-43819-x.

[17] L.-C. Li, M.-X. Li, M. Liu, B.-Y. Sun, C. Wang, J.-T. Huo, W.-H. Wang, Y.-H. Liu, Enhanced oxidation resistance of MoTaTiCrAl high entropy alloys by removal of Al, Science China Materials (2020) https://doi.org/10.1007/s40843-020-1332-2.

[18] F. Müller, B. Gorr, H.-J. Christ, H. Chen, A. Kauffmann, S. Laube, M. Heilmaier, Formation of complex intermetallic phases in novel refractory high-entropy alloys NbMoCrTiAl and TaMoCrTiAl: Thermodynamic assessment and experimental validation, Journal of Alloys and Compounds (2020) 155726. https://doi.org/10.1016/j.jallcom.2020.155726.

[19] F. Müller, B. Gorr, H.-J. Christ, H. Chen, A. Kauffmann, M. Heilmaier, Effect of microalloying with silicon on high temperature oxidation resistance of novel refractory high-entropy alloy Ta-Mo-Cr-Ti-Al, Materials at High Temperatures 35 (2018) 168–176. https://doi.org/10.1080/09603409.2017.1389115.

[20] H. Chen, A. Kauffmann, S. Seils, T. Boll, C.H. Liebscher, I. Harding, K.S. Kumar, D.V. Szabó, S. Schlabach, S. Kauffmann-Weiss, F. Müller, B. Gorr, H.-J. Christ, M. Heilmaier, Crystallographic ordering in a series of Al-containing refractory high entropy alloys Ta–Nb–Mo–Cr–Ti–Al, Acta Materialia 176 (2019) 123–133. https://doi.org/10.1016/j.actamat.2019.07.001.

[21] J.B. Nelson, D.P. Riley, An experimental investigation of extrapolation methods in the derivation of accurate unit-cell dimensions of crystals, Proceedings of the Physical Society 57 (1945) 160–177. https://doi.org/10.1088/0959-5309/57/3/302.

[22] S. Laube, H. Chen, A. Kauffmann, S. Schellert, F. Müller, B. Gorr, J. Müller, B. Butz, H.-J. Christ, M. Heilmaier, Controlling crystallographic ordering in Mo–Cr–Ti–Al high entropy alloys to enhance ductility, Journal of Alloys and Compounds 823 (2020) 153805. https://doi.org/10.1016/j.jallcom.2020.153805.

[23] W. Wong-Ng, H.F. McMurdie, B. Paretzkin, C.R. Hubbard, A.L. Dragoo, Standard X-Ray Diffraction Powder Patterns of Fourteen Ceramic Phases, Powder Diffraction 3 (1988) 252. https://doi.org/10.1017/s0885715600013385.

[24] W. Ren, F. Ouyang, B. Ding, Y. Zhong, J. Yu, Z. Ren, L. Zhou, The influence of $CrTaO_4$ layer on the oxidation behavior of a directionally-solidified nickel-based superalloy at 850–900 °C, Journal of Alloys and Compounds 724 (2017) 565–574. https://doi.org/10.1016/j.jallcom.2017.07.066.

[25] D. J. Young, High temperature oxidation and corrosion of metals, second edition, Elsevier Science, Amsterdam, 2016.

[26] P. Kofstad, High temperature oxidation of metals, John Wiley & Sons, INC., New York, 1966.

[27] P. Massard, J.C. Bernier, A. Michel, Effet Jahn-Teller dans le système Ta_2CrO_6-$TaCrO_4$, Journal of Solid State Chemistry 4 (1972) 269–274. https://doi.org/10.1016/0022-4596(72)90116-8.

[28] F. Schlottig, J. Schreckenbach, G. Marx, Preparation and characterisation of chromium and sodium tantalate layers by anodic spark deposition, Fresenius' Journal of Analytical Chemistry 363 (1999) 209–211. https://doi.org/10.1007/s002160051174.

[29] M.P. Brady, P.F. Tortorelli, L.R. Walker, Correlation of alloy microstructure with oxidation behavior in chromia-forming intermetallic-reinforced Cr alloys, Materials at High Temperatures 17 (2000) 235–243. https://doi.org/10.3184/096034000783640983.

[30] S.-J. Park, S.-M. Seo, Y.-S. Yoo, H.-W. Jeong, H. Jang, Effects of Al and Ta on the high temperature oxidation of Ni-based superalloys, Corrosion Science 90 (2015) 305–312. https://doi.org/10.1016/j.corsci.2014.10.025.

[31] H.-S. Kim, S.-J. Park, S.-M. Seo, Y.-S. Yoo, H.-W. Jeong, H. Jang, High temperature oxidation resistance of Ni-(5~13)Co-(10~16)Cr-(5~9)W-5Al-(1~1.5)Ti-(3~6)Ta alloys, Metals and Materials International 22 (2016) 789–796. https://doi.org/10.1007/s12540-016-6305-1.

[32] A. Jalowicka, W. Nowak, D. Naumenko, L. Singheiser, W.J. Quadakkers, Effect of nickel base superalloy composition on oxidation resistance in SO_2 containing, high pO_2 environments, Materials and Corrosion 65 (2014) 178–187. https://doi.org/10.1002/maco.201307299.

[33] K.-C. Lo, H. Murakami, J.-W. Yeh, A.-C. Yeh, Oxidation behaviour of a novel refractory high entropy alloy at elevated temperatures, Intermetallics 119 (2020) 106711. https://doi.org/10.1016/j.intermet.2020.106711.

[34] J. Li, Y. Chen, Y. Li, Z. Bai, K. Wang, Influence of aluminium addition on oxidation resistance of Ta-W alloy, Powder Metallurgy 62 (2019) 322–330. https://doi.org/10.1080/00325899.2019.1662559.

[35] A. Petersen, H. Müller-Buschbaum, Ein Beitrag über Oxide vom Typ AMO_4 ($A = Ti^{3+}$, Cr^{3+}; $M = Nb^{5+}$, Ta^{5+}), Journal of inorganic and General Chemistry 609 (1992) 51–54. https://doi.org/10.1002/zaac.19926090309.

[36] R. Mani, S.N. Achary, K.R. Chakraborty, S.K. Deshpande, J.E. Joy, A. Nag, J. Gopalakrishnan, A.K. Tyagi, $FeTiTaO_6$: A Lead-Free Relaxor Ferroelectric Based on the Rutile Structure, Adv. Mater. 20 (2008) 1348–1352. https://doi.org/10.1002/adma.200701940.

[37] L. Qin, Y. Pei, S. Li, X. Zhao, S. Gong, H. Xu, Role of volatilization of molybdenum oxides during the cyclic oxidation of high-Mo containing Ni-based single crystal superalloys, Corrosion Science 129 (2017) 192–204. https://doi.org/10.1016/j.corsci.2017.08.025.

[38] S.-J. Park, S.-M. Seo, Y.-S. Yoo, H.-W. Jeong, H. Jang, Effects of Cr, W, and Mo on the high temperature oxidation of Ni-Based superalloys, Materials 12 (2019) 2934. https://doi.org/10.3390/ma12182934.

[39] M. Azim, B. Gorr, H.-J. Christ, M. Heilmaier, U. Koch, M. Engelhard, Characterization of oxidation kinetics of Mo–Si–B-based materials, Oxidation of Metals 87 (2017) 89–108. https://doi.org/10.1007/s11085-016-9659-3.

[40] J. Emsley, The elements, third edition, Clarendon Press, Oxford, 1998.

Figure captions

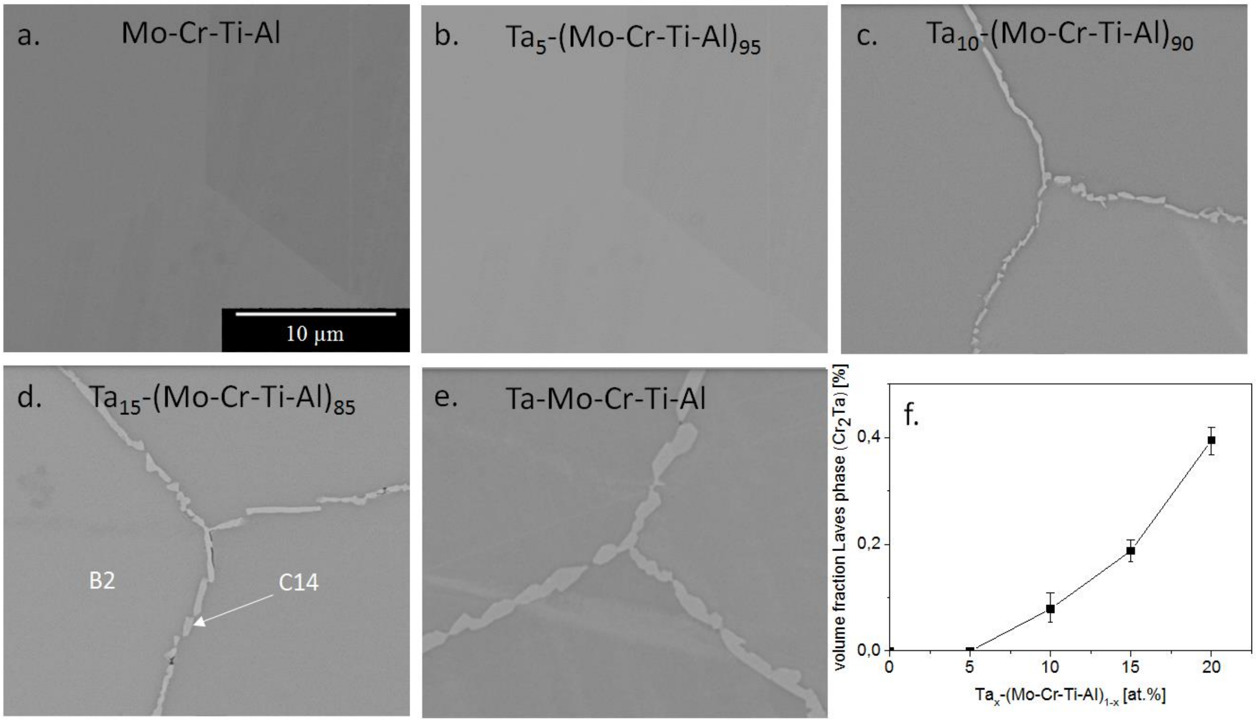

Fig. 1 BSE micrographs of the alloys after homogenization and cooling: (a.) Mo-Cr-Ti-Al , (b.) Ta$_5$-(Mo-Cr-Ti-Al)$_{95}$, (c.) Ta$_{10}$-(Mo-Cr-Ti-Al)$_{90}$, (d.)Ta$_{15}$-(Mo-Cr-Ti-Al)$_{85}$ and (e.) Ta-Mo-Cr-Ti-Al. (f.) Volume fraction of the C14 Laves phase as a function of the Ta contraction (in at.%) in xTa-Mo-Cr-Ti-Al. All BSE micrographs are taken at the same magnification.

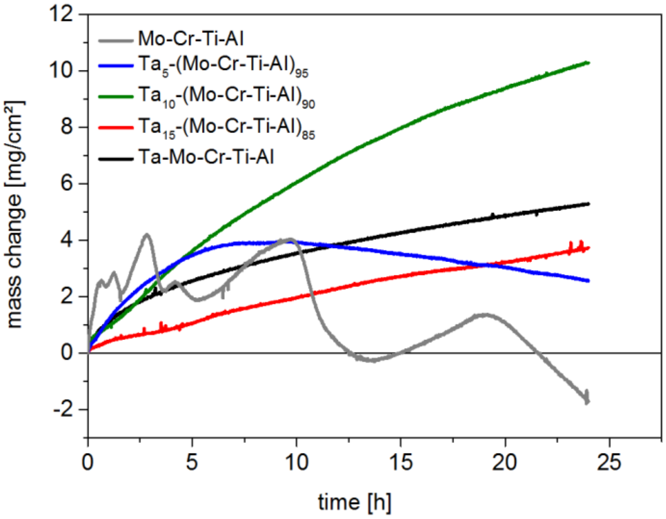

Fig. 2 Specific mass change as a function of time for Ta$_x$-(Mo-Cr-Ti-Al)$_{1-x}$ (x = 0; 5; 10; 15; 20 at.%) during isothermal exposure to air at 1200°C for 24h.

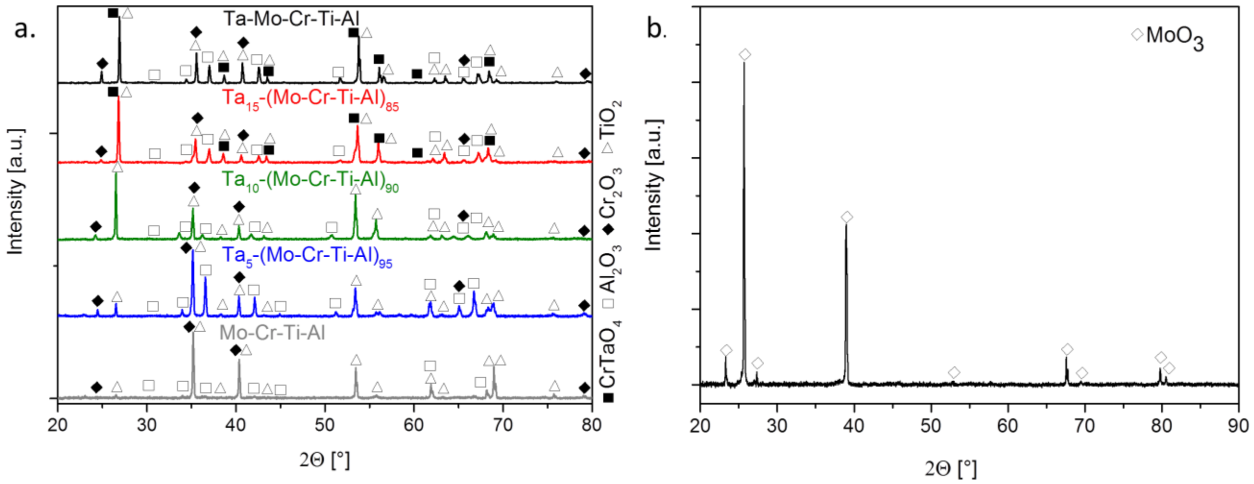

Fig. 3 Results of XRD analysis of (a.) Ta$_x$-(Mo-Cr-Ti-Al)$_{1-x}$ (x=5; 10; 15; 20 at.%) after 24h oxidation in air at 1200°C and (b.) substances taken off the platinum wire after 24h oxidation of the alloy Ta$_{15}$-(Mo-Cr-Ti-Al)$_{85}$ at 1200°C.

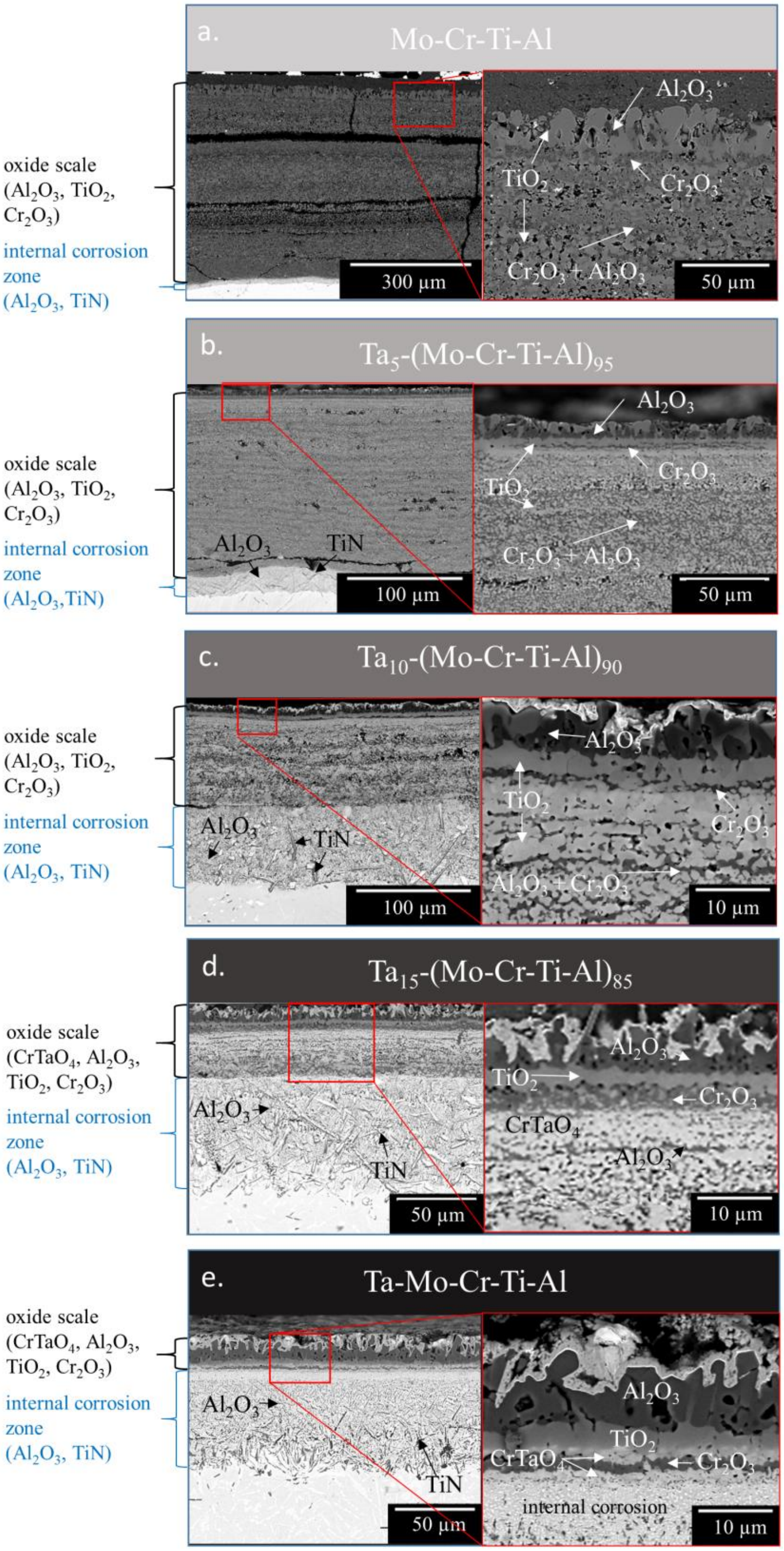

Fig. 4 Comparison of the BSE micrographs of: (a.) Mo-Cr-Ti-Al, (b.) Ta_5-(Mo-Cr-Ti-Al)$_{95}$, (c.) Ta_{10}-(Mo-Cr-Ti-Al)$_{90}$, (d.) Ta_{15}-(Mo-Cr-Ti-Al)$_{85}$ and (e.) Ta-Mo-Cr-Ti-Al after 24h of exposure to air at 1200°C. On the left side an overview micrograph and on the right side a detailed micrograph of the oxide layer highlighted in red on the left side. Contrast definitions in the oxide scale: bright contrast $CrTaO_4$, medium contrast TiO_2 and dark contrast Al_2O_3 and Cr_2O_3; in zone of internal corrosion the spherical Al_2O_3 particles yield a medium contrast and the needle-shaped TiN exhibits a dark contrast.

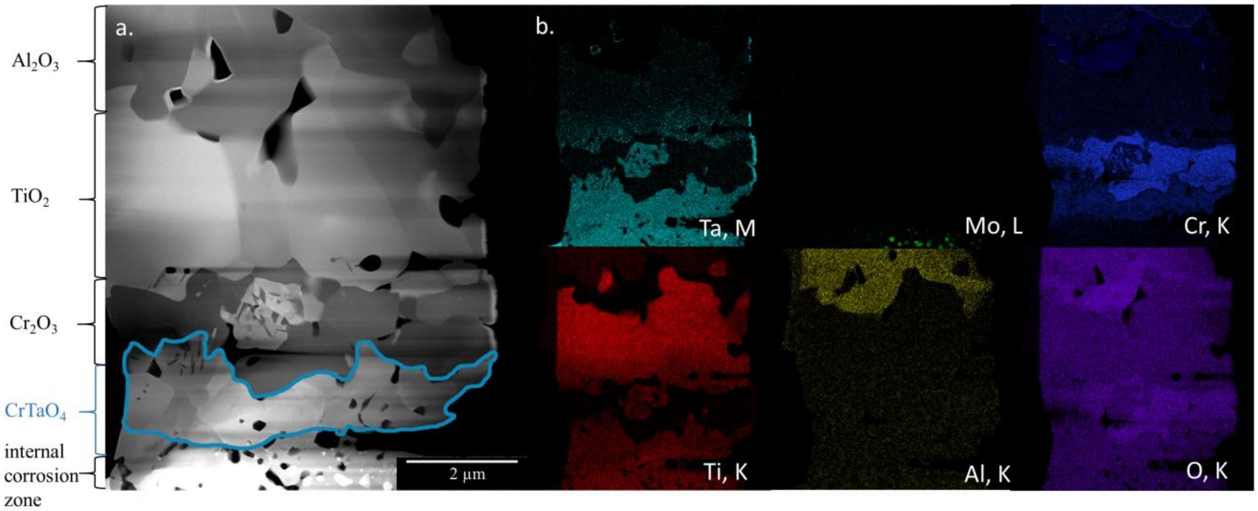

Fig. 5 Detailed micrographs of oxide scale formed on equiatomic Ta-Mo-Cr-Ti-Al after 24h exposure to air at 1200°C; (a) TEM lamella with highlighted $CrTaO_4$ highlighted in green (STEM-HAADF image), (b) EDX-analysis of the oxide scale shown (a.)

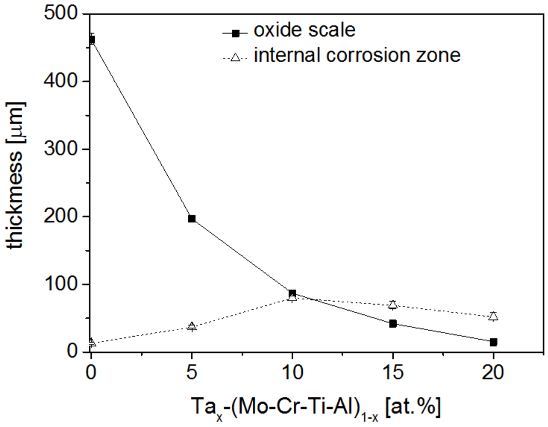

Fig. 6 Thicknesses of the oxide scale and the internal corrosion zone as a function of the Ta concentration in the alloys Ta_x-(Mo-Cr-Ti-Al)$_{1-x}$ (x = 0; 5; 10; 15; 20 at.%) after 24h oxidation in air at 1200°C.

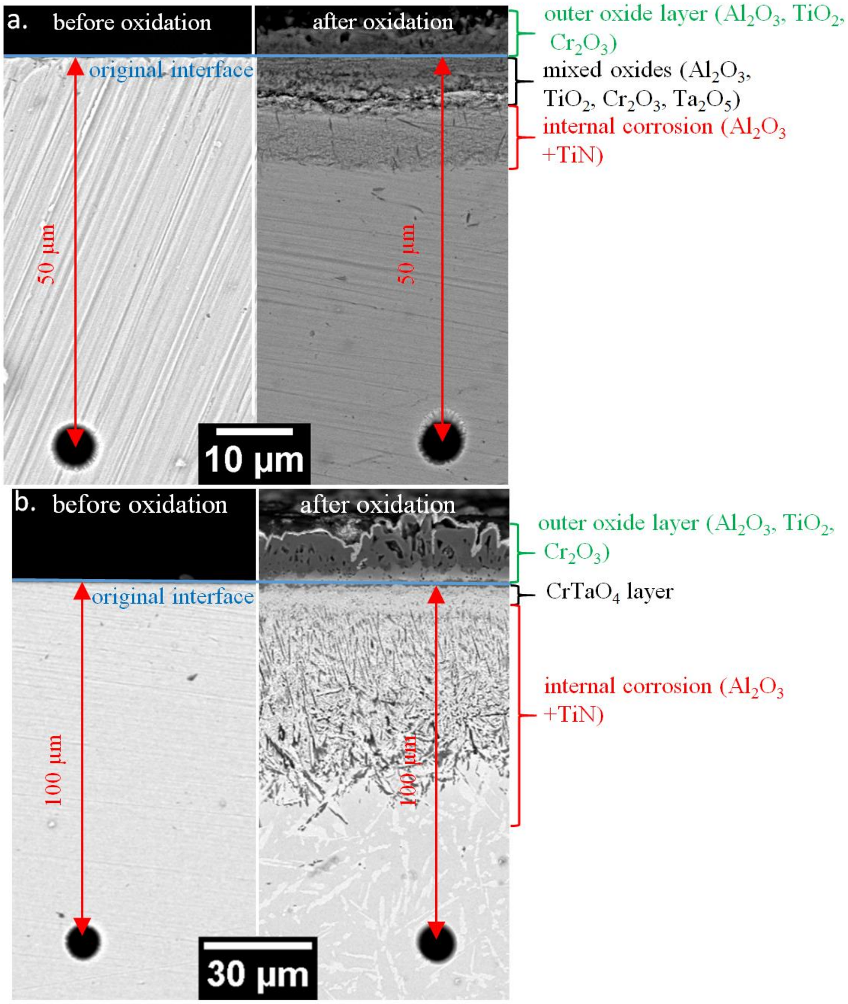

Fig. 7 Micrographs of the FIB marker experiments; (a.) Ta_5-(Mo-Cr-Ti-Al)$_{95}$ before (left) and after (right) oxidation for 30 min at 1200°C and (b.) Ta-Mo-Cr-Ti-Al before and after oxidation for 24h at 1200°C.

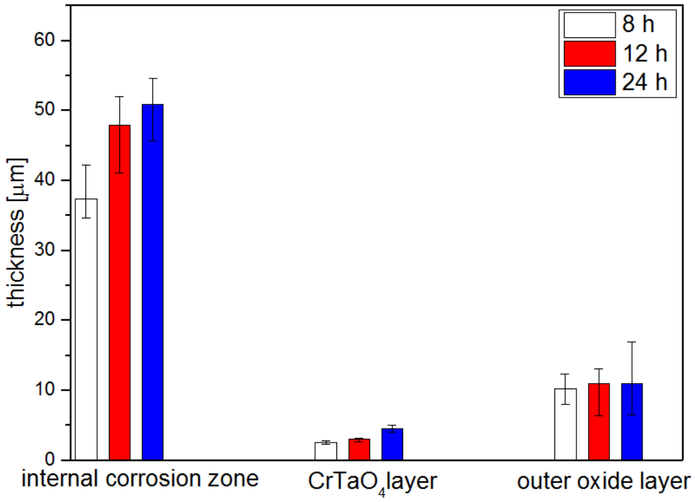

Fig. 8 Thicknesses of the zone of internal corrosion, $CrTaO_4$ scale and the outer oxide layer consisting of Al_2O_3, TiO_2, Cr_2O_3 formed on Ta-Mo-Cr-Ti-Al after oxidation for 8h, 12h, 24h at 1200°C.

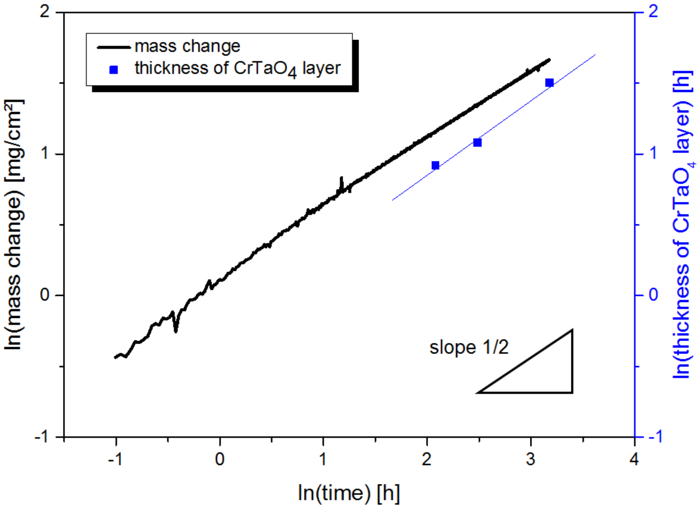

Fig. 9 Double logarithmic plot of the mass change (on the left y axis, in black) and the thickness of the $CrTaO_4$ layer (on the right y axis, in blue) against time of the equiatomic Ta-Mo-Cr-Ti-Al alloy during isothermal air exposure at 1200°C.

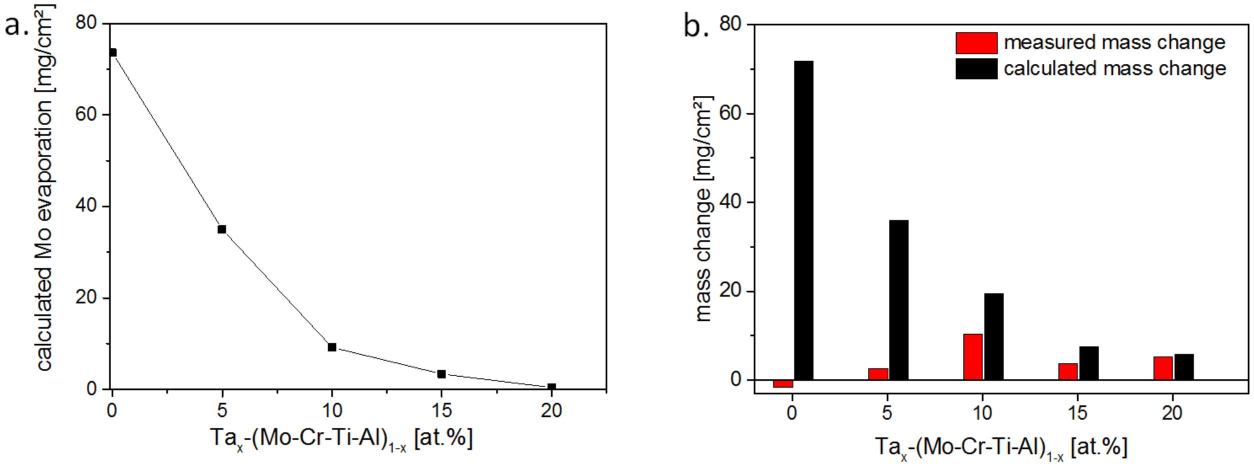

Fig. 10 MoO_3 evaporation during oxidation of alloys $(Ta)_x$-(Mo-Cr-Ti-Al)$_{1-x}$ (x = 0; 5; 10; 15; 20 at.%) for 24h at 1200°C: (a.) calculated Mo mass loss and (b.) comparison of the measured and calculated mass change (comparison is performed for the oxidation time of 24h).

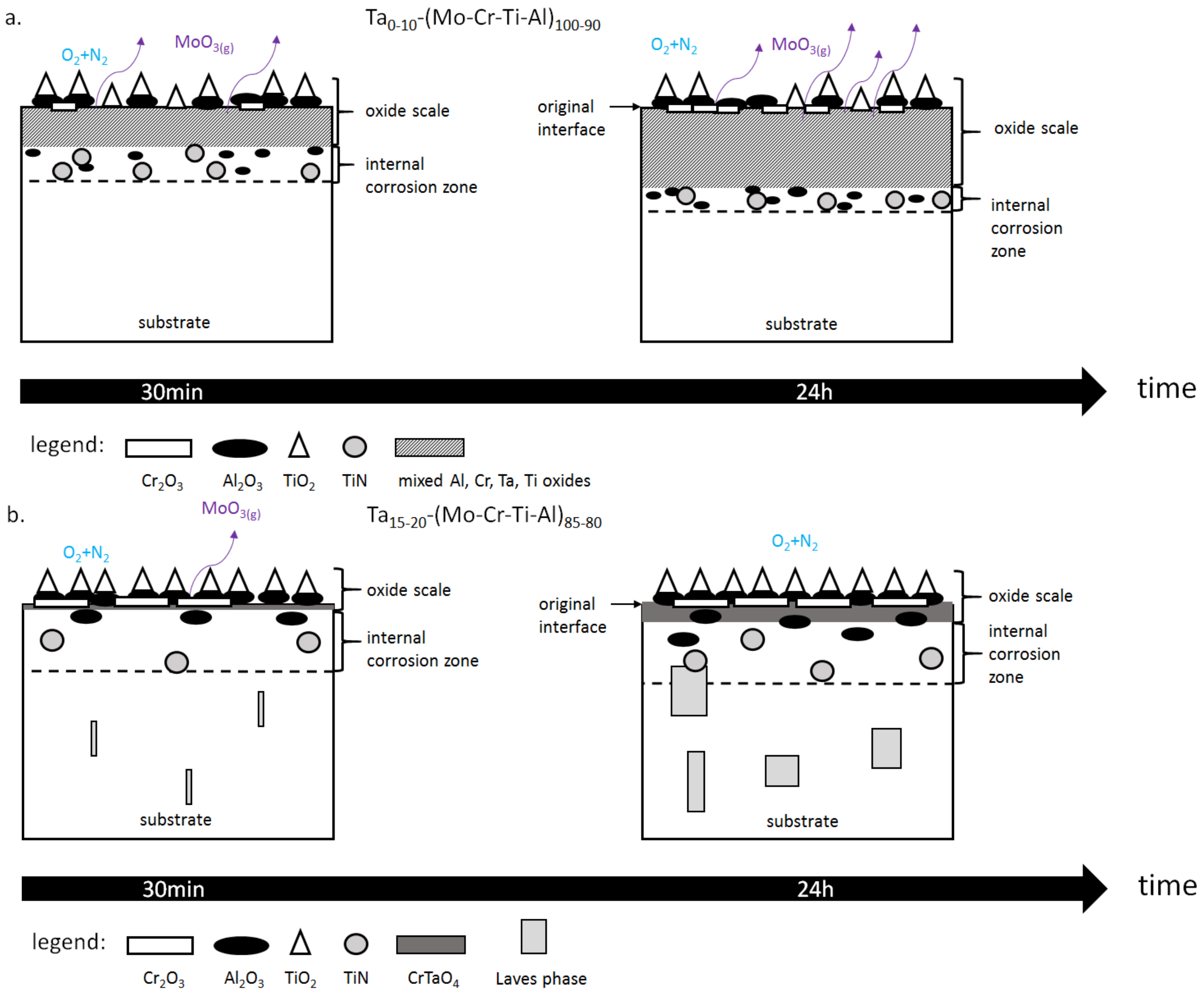

Fig. 11 Schematic representation of oxidation mechanisms of (a.) Ta_{0-10}-(Mo-Cr-Ti-Al)$_{100-90}$ (in at.%) and (b.) Ta_{15-20}-(Mo-Cr-Ti-Al)$_{85-80}$ (in at.%).

Table captions

Table 1: Chemical composition $\bar{x}_i$ [at.%] of investigated alloys in annealed condition. The chemical compositions of the Mo-Cr-Ti-Al and Ta-Mo-Cr-Ti-Al were taken from [20] and correspond to the same charges.

composition	**heat treatment**	**chemical compositions $\bar{x}_i$ of the investigated alloys [at.%]; * denotes ICP-OES, † indicates standard-related EDX.**				
		Ta	**Mo**	**Cr**	**Ti**	**Al**
Mo-Cr-Ti-Al*****	1200°C, 20h	-	24.8	24.9	24.9	25.4
Ta_5-$(Mo$-Cr-Ti-$Al)_{95}$†	1500°C, 20h	5.1	23.5	23.8	23.7	23.9
Ta_{10}-$(Mo$-Cr-Ti-$Al)_{90}$†	1500°C, 20h	10.2	22.3	22.4	22.7	22.4
Ta_{15}-$(Mo$-Cr-Ti-$Al)_{85}$†	1500°C, 20h	14.8	21.4	21.3	21.1	21.4
Ta-Mo-Cr-Ti-Al*****	1500°C, 20h	20.1	19.5	19.8	20.4	20.2

Supplementary Material

Material S1

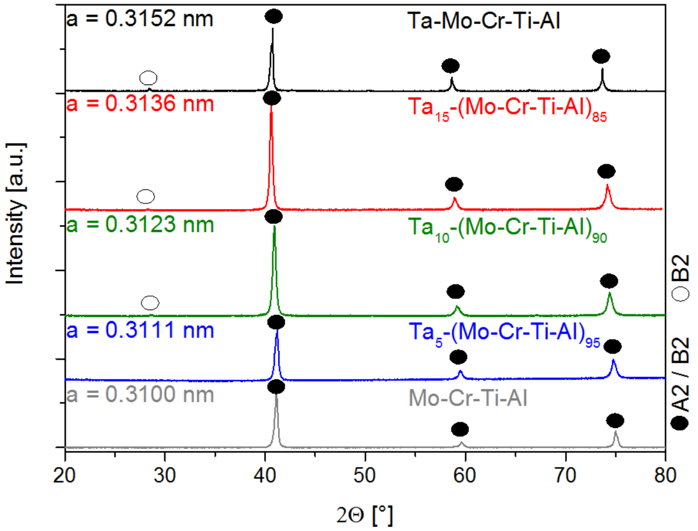

Fig. S. 1 Powder XRD pattern of the investigated alloys after 20h homogenization: Ta$_x$-(Mo-Cr-Ti-Al)$_{1-x}$ (x=5; 10; 15; 20 at.%) at 1500°C and Mo-Cr-Ti-Al at 1200°C. The alloys correspond to the same batch as mentioned in the respective reference. Closed circles indicate A2 / B2 Bragg peaks, open circles highlight visible B2 Bragg peaks. The patterns are offset in order to allow interpretation of otherwise overlapping curves.

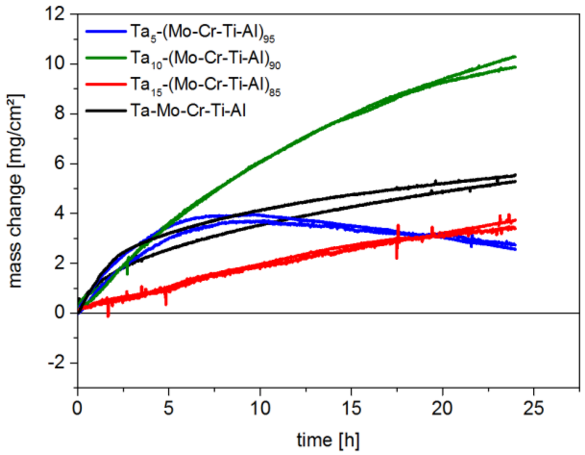

Fig. S. 2 Specific mass change as a function of time for Ta$_x$-(Mo-Cr-Ti-Al)$_{1-x}$ (x=5; 10; 15; 20 at.%) during isothermal exposure to air at 1200°C for 24h. Two samples per composition are displayed to highlight the reproducibility of the experiments.

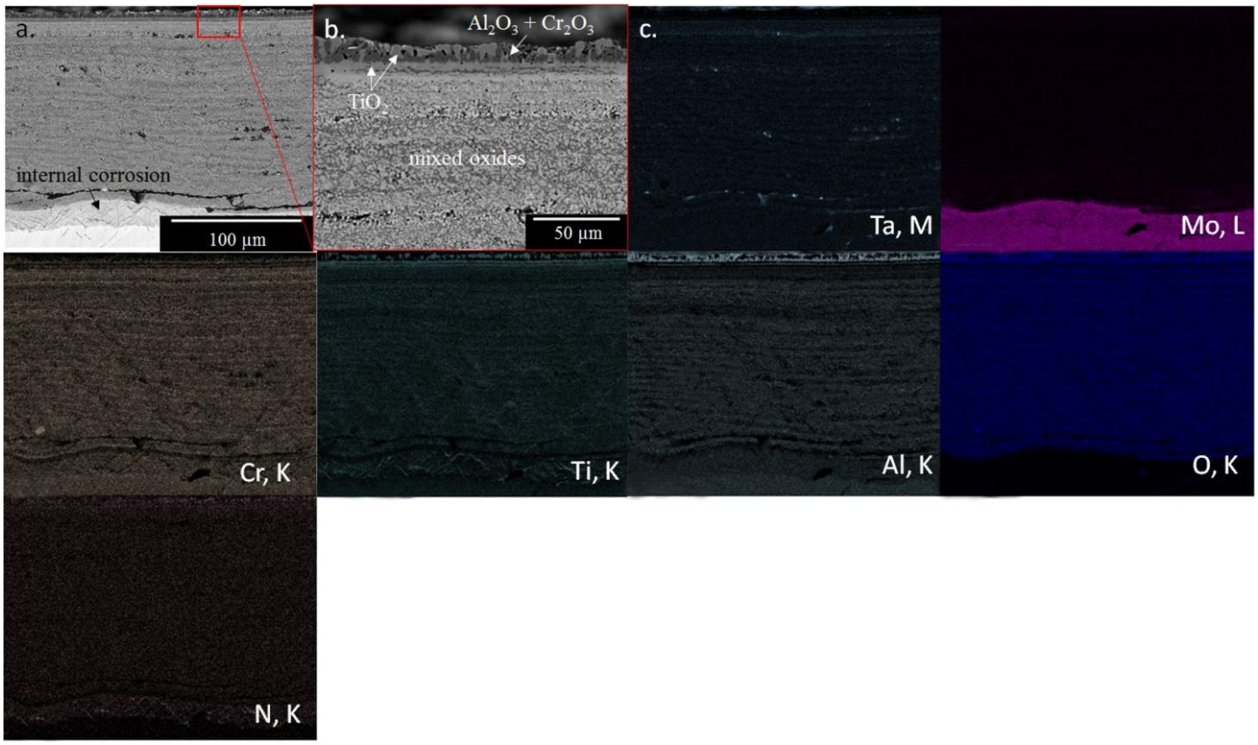

Fig. S. 3 Oxide scale formed on Ta_5-(Mo-Cr-Ti-Al)$_{95}$ after 24h exposure to air at 1200°C; (a) cross-section (BSE mode), (b) details of the interface oxide/air and (c) EDX-analysis of the oxide scale shown (a.)

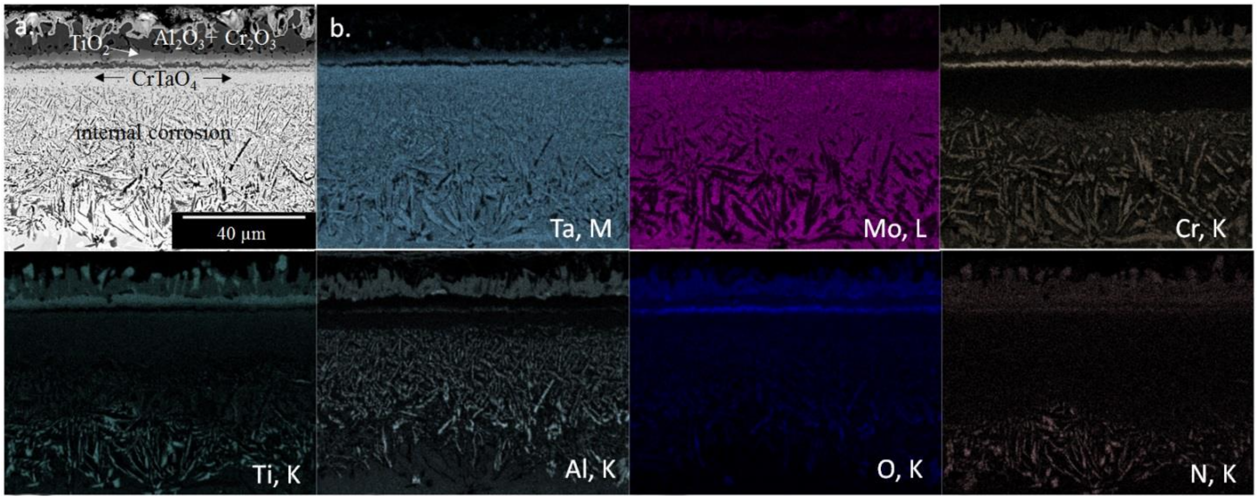

Fig. S. 4 Oxide scale formed on equiatomic Ta-Mo-Cr-Ti-Al after 24h exposure to air at 1200°C; (a) cross-section (BSE mode), (b) EDX-analysis of the oxide scale shown (a.)

Material S2 ***Method to determine Mo mass loss due to evaporation of MoO_3***

The current calculation approach is largely based on the method described in Ref. [39] and applied to determine the amount of material affected by oxidation. In addition, this method allows a quantitative determination of the mass loss of refractory metals due to the evaporation of their oxides. Thus, the thermogravimetrically recorded mass change, which represents the sum of the positive (oxygen uptake) and the negative contributions (oxide evaporation), can be corrected taking into account the negative mass change.

The main idea of the current approach is to determine the volume of the original sample in which Mo oxidizes, converts to MoO_3 and finally escapes through the oxide scale. Our previous investigations showed that alloys within the system Ta-Mo-Cr-Ti-Al form multi-layer scales, whereas some oxides grow outward, while another inward with respect to the original sample surface [14]. The volume of the inwardly grown oxide scale represents the volume of the Mo-free part of the oxidizes sample. This volume, which should be determined, is schematically represented in Fig. S. 5 by the medium dark contrast. It is defined by two interfaces, namely by the original sample surface and the interface oxide/substrate below which Mo is still present in the nominal concentration. Taking into account the mole fraction of Mo in the alloy, the weight of Mo in this particular volume can be determined which is nearly equal to that lost during oxidation as a result of MoO_3 evaporation.

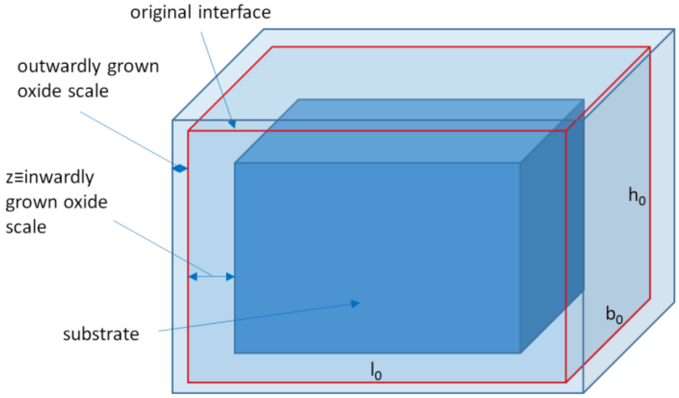

Fig. S. 5 Schematic representation of the method determining the Mo loss in an sample as a result of MoO_3 vaporization.

The following assumptions have been made to calculate the Mo loss in the alloys Ta_x-(Mo-Cr-Ti-Al)$_{1-x}$ (x = 0; 5; 10; 15; 20 at.%):

- (i.) the scatter of the oxide scale thickness is negligible (average thickness is taken into account in the calculation)
- (ii.) Mo evaporates completely in the area between the original surface and the interface oxide/substrate
- (iii.) enrichment or depletion of Mo at the interface of oxides/substrates are negligible
- (iv.) homogeneous distribution of the elements in the inwardly grown oxide layer and the alloy
- (v.) single-phase alloys (negligible amount of second phase)
- (vi.) defect-free (pores etc.) alloys and oxide scales

The mathematical description of Mo loss is given by Eq. (1) where length l_o, width w_o and height h_o describe the geometry of the sample before oxidation, $\bar{\rho}_{alloy}$ is the theoretical alloy density and w_{Mo}denotes the Mo mass fraction in the alloy. In equation (1), *z* represents the thickness of the inwardly grown oxide scales and, therefore, the Mo-free part of the oxidized sample. Taking into account the knowledge of the original sample surface (see Fig. 7 as well the corresponding explanation), *z* can be determined using the BSE/EDX images (as an example see Fig. S. 3).

$$\frac{m_{Mo}}{A} = \frac{[l_0 \cdot b_0 \cdot h_0 - (l_0 - 2 \cdot z) \cdot (b_0 - 2 \cdot z) \cdot (h_0 - 2 \cdot z)] \cdot \bar{\rho}_{alloy} \cdot w_{Mo}}{2 \cdot (\, l_o \cdot \, b_o + \, l_o \cdot \, h_o + \, b_o \cdot \, h_o)} \qquad (1)$$

The theoretical density $\bar{\rho}_{alloy}$ is calculated using the Eq. (2).

$$\bar{\rho}_{alloy} = \frac{\bar{M}_{alloy} \cdot A_{EC}}{{a_{alloy}}^3} \qquad (2)$$

Due to the low volume fraction (0.4 vol.%) of the Laves phase, the amount was neglected and the density can be determined in a reasonable approximation using Eq. (2). In equation (2), $\bar{M}_{alloy}$ represents the average atomic weight of the alloy, $A_{EC} = 2$ is the number of atoms in the unit cell with bcc crystal structure, a_{alloy} is lattice parameter of the alloy, respectively. The lattice parameters were determined from the XRD results (Fig. S. 1). In addition, the lattice parameters were adjusted using TEM-SAD images. Fig. S. 6 exhibits the TEM-SAD image of Ta_5-(Mo-Cr-Ti-Al)$_{95}$ in [011] zone axis as an example. In all cases, the lattice parameters determined by both methods are in excellent agreement The deviation is approximately 0.0005 nm.

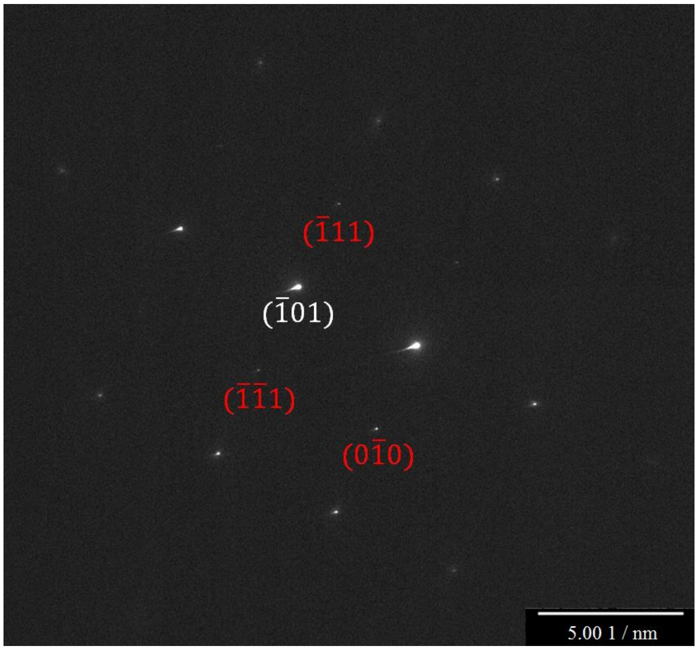

Fig. S. 6 Selected Area Diffraction pattern of Ta_5-(Mo-Cr-Ti-Al)$_{95}$ in [011] Zone axis. Superlattice spots corresponding to the B2 crystal structure are labeled in red.

$$\bar{M}_{alloy} = \sum_{i=1}^{n} M_i \cdot \bar{x}_i \tag{3}$$

Equation (3) describes the $\bar{M}_{alloy}$ average atomic weight of the alloy, whereby M_i is the molar weight of each element and x_i is the mole fraction of elements in the alloy (see Table 2).

Using the data from the Table 2, the weight fraction of Mo w_{Mo} in the alloy is also calculated by applying the following equation (4):

$$w_i = \frac{M_i \cdot x_i}{\sum_{n=1}^{n} M_n \cdot x_n} \tag{4}$$

The index n in turn acts as a common running index for the summations and includes i.

Table 2: molar weight of each element M_i [40] and the mole fraction x_i of the elements in Ta_5-(Mo-Cr-Ti-Al)$_{95}$ determined by EDX analyses (see Table 1 for reference).

element i	**molar weight M_i [g/mol]**	**mole fraction x_i of the elements in the alloy**
Ta	180.947 [40]	0.051
Mo	95.95 [40]	0.235
Cr	51.9961 [40]	0.238
Ti	47.867 [40]	0.237
Al	26.9815 [40]	0.239

Table 3 shows the input data to calculate the Mo mass loss for the alloy Ta$_5$-(Mo-Cr-Ti-Al)$_{95}$. The calculation of the Mo mass loss in the alloy Ta$_5$-(Mo-Cr-Ti-Al)$_{95}$ after 24h oxidation at 1200°C yields approximately 35 mg/cm².

Table 3 Parameter used to calculate the Mo loss in the alloy Ta$_5$-(Mo-Cr-Ti-Al)$_{95}$ and the corresponding applied method.

parameter	**method**
$l_o = 0.402\ cm$	measured by caliper gauge
$w_o = 0.309\ cm$	measured by caliper gauge
$h_o = 0.341\ cm$	measured by caliper gauge
$z = 0.0153\ cm$	measured using BSE/EDX images
$a_{alloy} = 0.311\ nm$	determined by XRD pattern
$\bar{\rho}_{alloy} = \ 6.84\ \mathrm{g/cm^3}$	determined using equation (3) and values from Table 2
$w_{Mo} = \ 0.364$	determined using equation (4) and values from Table 2